Astronomy & Astrophysics

Deep search for hydrogen peroxide toward pre- and protostellar objects

Testing the pathway of grain surface water formation

G. W. Fuchs[1], D. Witsch[1], D. Herberth[1], M. Kempkes[1], B. Stanclik[1], J. Chantzos[2], H. Linnartz[3],
K. Menten[4], and T. F. Giesen[1]

[1] Institute of Physics, University Kassel, Heinrich-Plett Str. 40, 34132 Kassel, Germany
   e-mail: fuchs@physik.uni-kassel.de
[2] Max-Planck-Institute for Extraterrestrial Physics (MPE), Giessenbachstraße 1, 85748 Garching, Germany
[3] Laboratory for Astrophysics, Leiden Observatory, Leiden University, PO Box 9513, 2300 RA Leiden, The Netherlands
[4] Max-Planck-Institut für Radio Astronomy (MPIfR), Auf dem Hügel 69, 53121 Bonn, Germany

ABSTRACT

Context. In the laboratory, hydrogen peroxide (HOOH) was proven to be an intermediate product in the solid-state reaction scheme that leads to the formation of water on icy dust grains. When HOOH desorbs from the icy grains, it can be detected in the gas phase. In combination with water detections, it may provide additional information on the water reaction network. Hydrogen peroxide has previously been found toward ρ Oph A. However, further searches for this molecule in other sources failed. Hydrogen peroxide plays a fundamental role in the understanding of solid-state water formation and the overall water reservoir in young stellar objects (YSOs). Without further HOOH detections, it is difficult to assess and develop suitable chemical models that properly take into account the formation of water on icy surfaces.
Aims. The objective of this work is to identify HOOH in YSOs and thereby constrain the grain surface water formation hypothesis.
Methods. Using an astrochemical model based on previous work in combination with a physical model of YSOs, the sources R CrA-IRS 5A, NGC C1333-IRAS 2A, L1551-IRS 5, and L1544 were identified as suitable candidates for an HOOH detection. Long integration times on the APEX 12 m and IRAM 30 m telescopes were applied to search for HOOH signatures in these sources.
Results. None of the four sources under investigation showed convincing spectral signatures of HOOH. The upper limit for HOOH abundance based on the noise level at the frequency positions of this molecule for the source R CrA-IRS 5A was close to the predicted value. For NGC 1333-IRAS 2A, L1544, and L1551-IRS 5, the model overestimated the hydrogen peroxide abundances.
Conclusions. HOOH remains an elusive molecule. With only one secure cosmic HOOH source detected so far, namely ρ Oph A, the chemical model parameters for this molecule cannot be sufficiently well determined or confirmed in existing models. Possible reasons for the nondetections of HOOH are discussed.

Key words. ISM: molecules – ISM: abundances – methods: observational – stars: formation – submillimeter: ISM – astrochemistry

1. Introduction

Water is the essence of life and is one of the most relevant molecules in the Universe. In star formation processes, H_2O plays an important role as coolant; in dense cold regions, water is the dominant constituent in ices coating cosmic grains; and generally, water can be used as a valuable physical diagnostic and evolutionary tracer (van Dishoeck et al. 2011). Its origin and abundance in space is at the core of fundamental questions that still lack conclusive answers. Three reaction schemes are commonly used to explain water formation in space (van Dishoeck et al. 2013; Hollenbach et al. 2009). In hot or radiation-exposed environments, gas-phase reactions dominate that are either based on high temperature (1) or ion-molecule reactions (2). In cold and radiatively well-shielded regions where ices form on cold dust grains, solid-state reactions (3) are at play. The latter mechanism is believed to dominate in the environments of star-forming regions. Dedicated observing programs such as the *Herschel*-WISH program (van Dishoeck et al. 2011) have investigated the abundance and occurrence of water in our Universe and

in our local galactic environment. In addition, laboratory data of chemical processes in interstellar ice analogs became available that helped to better understand the mechanisms of water formation on interstellar dust surfaces (Ioppolo et al. 2010). Laboratory studies showed that hydrogen peroxide (HOOH) acts as a prominent intermediate in the hydrogenation chain from oxygen allotropes (O, O_2, and O_3) to the formation of water (Ioppolo et al. 2008; Miyauchi et al. 2008; Oba et al. 2009; Dulieu et al. 2010; Cuppen et al. 2010; Romanzin et al. 2011). This also means that HOOH has the potential of acting as a tracer of solid-state reactions that result in the formation of water. This depends on the amount of HOOH that is present in the ice because it may fully react to form water, and it depends on the efficiency with which HOOH can be released into the gas phase after it is formed, for instance, through reactive desorption or dissociative desorption processes. In addition, the amount of observable HOOH may be reduced by gas phase processes that consume HOOH once it is released from the solid. The first point, that is the amount of solid-state HOOH, has been addressed by Smith et al. (2011) by investigating interstellar ices at 3.5, 7.0, and

11.3 μm where HOOH can be distinguished from water ices; see also Boudin et al. (1998). However, no conclusive evidence for HOOH as grain mantle constituent could be reported. At best, the 3.47 μm feature at the shoulder of the long-wavelength wing of the 3.08 μm water O–H stretching feature might be assumed to originate from HOOH (but possibly also from other molecules) and might thus be used to infer an upper limit, which would then be between 2 and 17%. However, already in 2011, gas-phase HOOH was identified toward the star-forming region ρ Oph A (Bergman et al. 2011a). Du et al. (2012) developed a detailed model based on chemical surface reactions and subsequent desorption processes to explain these observations. They also predicted that HO$_2$ exists in ρ Oph A in sufficient amounts that were subsequently detected by Parise et al. (2012). Based on these first successes, a survey toward various inter- and circumstellar environments, including star-forming regions at various phases of stellar evolution, was started by Parise and colleagues to search for further sources of hydrogen peroxide. Surprisingly, it was not possible to identify HOOH in any of these targets (Parise et al. 2014). Liseau & Larsson (2015) reported a tentative detection of hydrogen peroxide toward OMC-1, but because the millimeter spectrum in this source is very dense, a firm assignment is still pending. Because water can be seen in many star-forming regions, including those investigated by Parise et al. (2014), it remains puzzling why HOOH is so difficult to observe. Parise et al. argued that ρ Oph A appears to be a somewhat special source with favorable conditions for an HOOH detection mainly because the bulk of gas can be found under constant conditions at moderate temperatures of around 20–30 K. The heating source responsible for these temperatures is the nearby star S1 (a close binary system of the classes B4 and K). It has also been pointed out that sources in which the molecule O$_2$ has been observed would be ideal candidates for HOOH detections (Liseau & Larsson 2015) because molecular oxygen is a direct precursor molecule for HOOH on grain surfaces (Cuppen et al. 2010). However, O$_2$ is difficult to detect, and it is commonly believed that it is not a major repository of oxygen in molecular clouds. In only two sources has molecular oxygen been identified so far, namely ρ Oph A and Orion A (Larsson et al. 2007; Liseau et al. 2012; Goldsmith et al. 2011; Chen et al. 2014), and many further attempts to find it in the gas phase have failed (Goldsmith et al. 2000; Melnick & Bergin 2005; Yıldız et al. 2013; Wirström et al. 2016), as did the attempts to find it in solid form (Van den Bussche et al. 1999; Tielens 2000).

In the model by Du et al. (2012) a desorption mechanism is included that is based on the release of excess energy during the molecule formation. This concept has also been applied by Cazaux et al. (2016) and Minissale et al. (2016). Initially, and already including gas- and solid-phase reactions, Du et al. (2012) constrained themselves to stationary and constant physical conditions in their model. Later, they applied the model to account for spherical symmetric problems such as in NGC 1333-IRAS 4A (Parise et al. 2014). In the latter case, the HOOH nondetection disagrees with their prediction, but at the same time, their analysis emphasized the critical role of the local physical conditions (e.g., density and temperature) and age of the source, neither of which were well determined. Their model has therefore not been unequivocally confirmed so far.

Our aim is to estimate the HOOH abundance during the early phases of young stellar objects (YSOs) by combining the results of the chemical model from Du et al. (2012) with the assumption of a spherical gradient distribution of the density and temperature of these sources. YSOs in their various phases can be very complicated objects geometrically. However, for many purposes,

the assumption of spherical symmetry with density and temperature gradients that can be determined by spectral energy distribution (SED) analysis is often assumed to be sufficient to obtain good estimates of key parameters of the system (Ivezic & Elitzur 1997; Schoeier et al. 2002; Kristensen et al. 2012). We therefore combined the chemical model from Du et al. (2012) with simple geometrical assumptions of the YSO in our model. This "gradient model" will be described elsewhere (Fuchs et al. 2020). In brief, because the model assumes spherical symmetry, the YSO is divided into concentric shells, each of which has constant density and temperature. The density and temperature of each shell i at radius $r_{shell,i}$ is given by the functions $\rho_{shell,i} \sim r_{shell,i}^{-p}$ and $T_{shell,i} \sim r_{shell,i}^{-b}$, with p and b being specific source parameters that have been determined from SED observations. In each shell the chemistry starts with the same initial chemical composition, but then evolves differently over time according to the chemical model given by Du et al. (2012). The chemical model includes gas-phase and surface reactions, but particular attention was paid to the role of surface reactions, that is, the HOOH reaction pathway, in the water formation process. In this model, HOOH and O$_2$ are mainly formed on grain surfaces by hydrogenation of molecular oxygen via H + O$_2$ $\rightarrow$ O$_2$H, with the subsequent reactions H + O$_2$H $\rightarrow$ H$_2$O$_2$ and H + H$_2$O$_2$ $\rightarrow$ H$_2$O + OH. Alternative surface reaction routes are also considered, such as H + O $\rightarrow$ OH and H + OH $\rightarrow$ H$_2$O, but they do not result in comparable amounts of HOOH or H$_2$O. Using our gradient model, we predict the gas-phase abundance of HOOH in the close-by YSOs L1551-IRS 5, R CrA-IRS 5A, and NGC 1333-IRAS 2A, as well as in the pre-stellar core L1544. We compare our values with the astronomically observed values.

2. Astronomical sources

Based on an extensive list of pre- and protostellar objects (see Kristensen et al. 2012; Mottram et al. 2014), we selected sources that according to our model are the most promising candidates for a successful HOOH detection and that are within reach of either the APEX 12 m or the IRAM 30 m telescope. These sources are R CrA-IRS 5A, NGC 1333-IRAS 2A, and L1551-IRS 5. An additional source, the pre-stellar core L1544, was included for the following two reasons. First, our model shows that even at early stages, HOOH is expected to be produced. Second, L1544 shows water vapor emission in its cold inner core (7–10 K) where water should be frozen out onto grains (Caselli et al. 2012). A surprisingly effective desorption mechanism therefore appears to drive the water into the gas phase, and this may also apply to HOOH.

In all presented sources, water vapor has been observed in emission and for some also in absorption (Kristensen et al. 2012). Depending on the method and region (e.g., outer or inner envelope, jet), the reported H$_2$O abundance varies strongly. According to Kristensen et al. (2012), column densities of $N_{(H_2O)} > 10^{13}$ cm^{-2} are required to account for the absorption features of the ortho-H$_2$O transitions in the outer envelope seen by *Herschel*. Generally, the relative abundances [H$_2$O]/[H$_2$] inferred from absorption features appear to lie between $<10^{-11}$ for highly embedded sources and $>10^{-9}$ for less deeply embedded sources. However, NGC 13333-IRAS 2A is an exception with slightly higher relative abundances (see below). Investigations of similar sources by comparing CO/H$_2$O line ratios result in water abundances relative to H$_2$ of 10^{-7}–10^{-5} for low-density regions and 10^{-8}–10^{-6} for high-density areas (Franklin et al. 2008; Lefloch et al. 2010; Kristensen et al. 2012). It appears that water emission can be seen mainly in Class 0 objects by outflow components that

Table 1. Astronomical parameters of the investigated objects.

Source		RA(J2000) α	Dec(J2000) δ	v_{LSR} (km s^{-1})	Distance (pc)	Telescope	Reference
R CrA-IRS 5A	Protostar, Class 1	19 01 48.0	−36 57 21.6	5.7	130	APEX 12 m	[1]
					170		[2]
NGC 1333-IRAS 2A	Protostar, Class 0				220		[3]
Position 1		03 28 55.6	+31 14 37.1	7.7		APEX 12 m	[4]$^{(a)}$
Position 2		03 28 53.7	+31 14 28.0	7.7		APEX 12 m	
Position 3		03 28 56.2	+31 15 00.0	7.7		APEX 12 m	
L1551-IRS 5	Protostar, Class 1	04 31 19.10	+18 08 09.0	6.2	140	IRAM 30 m	[5]$^{(b)}$
L1544	Prestellar core	05 04 18.50	+25 11 10.0	7.2	140	IRAM 30 m	[6]$^{(c)}$

Notes. $^{(a)}$The use of three different positions for NGC 1333-IRAS 2A is motivated by the fact that during the original HOOH detection toward ρ Oph A, the strongest signal was observed between the SM1 and SM1N region and not at the respective CO peak positions, see Bergman et al. (2011a,b) . $^{(b)}$For recent source position data of L1551-IRS 5 using the VLA at 7 mm, see Villa et al. (2017). $^{(c)}$The L1544 position deviates from the dust peak position α: 05 04 17,21; δ: +25 10 42,8 and was chosen according to the CH$_3$OH maps from Bizzocchi et al. (2014).
References. [1] Peterson et al. (2011), [2] Nutter et al. (2005), [3] Bottinelli et al. (2007), [4] Wilkin et al. (2002), [5] Osorio et al. (2003), [6] Bizzocchi et al. (2014).

are caused by in-falling envelopes. Class 1 objects reveal only minor or no outflow features, and thus H$_2$O signals are generally weaker. Observational details of all four investigated sources are given in Table 1.

L1544 (prestellar core). This object is a star-less low-mass star-forming region in the constellation Taurus. The region is thought of as being on the point of becoming unstable, that is, starting star formation (Crapsi et al. 2005, 2007). A mapping of L1544 at 850 μm is presented in Shirley et al. (2000). L1544 can be modeled with a simple flat temperature and density distribution according to Caselli et al. (2002). The relative O$_2$ abundance has been shown to be [O$_2$]/[H$_2$] < 6.3×10^{-8} (Wirström et al. 2016). Water emission has been detected in this source (Caselli et al. 2012) with a column density N_{H_2O}(ortho + para) > 10^{13} cm^{-2} using the ortho-H$_2$O transition $1_{10}-1_{01}$, which was measured with an integrated line strength of $\int T_B \, dv =$ 5 mK km s^{-1}. This yields a relative water abundance [H$_2$O]/[H$_2$] < 1.4×10^{-10} (using N(H$_2$) $\simeq 7 \times 10^{22}$ cm^{-2}).

NGC 1333-IRAS 2A (Class 0). NGC 1333-IRAS 2A is a typical Class 0 object (Brinch et al. 2009) located in the constellation Perseus. The source has a complex structure with a clear indication of jet formation (Sandell et al. 1994; Wilkin et al. 2002; Engargiola & Plambeck 1999) and protostellar infall (Ward-Thompson et al. 1996). Maps and further information on shocks and the structure at small scales can be found in Jørgensen et al. (2004a,b). Because the structure is complex, we decided to investigate three spatially separated regions of this source. The reasoning behind this is also that Bergman et al. (2011a) did not find the peak intensity of HOOH toward the submillimeter sources SM1 or SM1N within the ρ Oph A complex, but instead found them in between these sources. It therefore seemed reasonable to investigate at least two further locations of the IRAS 2A region that are both differently positioned relative to the existing outflows, that is, position 2 and 3 are still in the vicinity of the central region where densities are still high but either off-center (position 2) or center-line to the north-south outflow. In the WISH/*Herschel* program, water emission at 557 GHz ($1_{10}-1_{01}$ transition) was found with $\int T_{mb}^{total} dv =$ 5.2 K km s^{-1} (Kristensen et al. 2012). The relative abundance was determined as [H$_2$O]/[H$_2$] $\sim 10^{-8}$ (Kristensen et al. 2010, 2012) based on absorption features.

R CrA-IRS 5A (Class 1). The source IRS 5 (Taylor & Storey 1984) is located in Corona Australis close to the star R CrA and is also known as SMM4, MMS12, or TS2.4 (see A.19 in Peterson et al. 2011). It is a binary system separated by ∼78 AU. The brighter source IRS 5a, is of spectral type K5–K7V, and is classified as a Class 1 YSO (Chen & Graham 1993; Nisini et al. 2005). In its direct vicinity (north) lies IRS 5N. SMA continuum measurements at 225 GHz suggest that the latter source is the driver of a CO outflow, whereas IRS 5a/b shows no features (Peterson et al. 2011). Water vapor has also been seen in emission at 557 GHz, with a line intensity of $\int T_{mb}^{total} dv =$ 3.8 K km s^{-1} (Kristensen et al. 2012). Schmalzl et al. (2014) reported a relative water vapor abundance of 1.7×10^{-8} (using $N_{Hydrogen} \simeq 4.9 \times 10^{22}$ cm^{-2}).

L1551-IRS 5 (Class 1). The close-by YSO L1551 is a Class 1 source with a core binary system in the Taurus molecular cloud complex (Osorio et al. 2003; Lee et al. 2014; Ainsworth et al. 2016). Because of its proximity, luminosity, and accessibility for the IRAM 30 m telescope, this source was considered to be a good candidate for our purposes. In earlier studies (White et al. 2000) no water emission was found toward IRS 5. However, using the *Herschel* space observatory, H$_2$O at 557 GHz could be detected, and this resulted in an integrated line intensity of $\int T_{mb}^{total} dv =$ 0.7 K km s^{-1} (Kristensen et al. 2012). The relative gas-phase water abundance is about 4×10^{-10} (using $N_{Hydrogen} \simeq 7.4 \times 10^{23}$ cm^{-2}), see Schmalzl et al. (2014).

3. Observations

The observations were performed using two telescopes: the APEX 12 m and IRAM 30 m telescopes. We used the APEX 12 m telescope in Chile to observe R CrA-IRS 5A and NGC 1333-IRAS 2A between September 8 and 19, 2015, during nine observational runs[1]. Observations were made at 217.0–221.0 GHz, 249.9–253.9 GHz, and 316.2–320.2 GHz with a total on-source time of 10 hours; see Table 2 for more details. The precipitable water vapor (pwv) values were between 0.8 mm and 2.3 mm but below 1.3 mm most of the time. We used the HET230 and HET345 (each with 4 GHz bandwidth) heterodyne

---
[1] APEX 12 m project E-096.C-0780A-2015.

Table 2. Observational details.

Frequency bands	rms [a]	Weather cond.	T_{sys}
(GHz)	(mK)	τ	(K)
APEX 12 m, position switching			
217.000–221.000	7.8–12.8	0.071–0.147	160–173
249.914–253.915	23.3	0.139	208
316.222–320.223	12.3–47.6	0.151–0.309	240–296
IRAM 30 m, position switching			
83.886–91.665	6.6	0.057	150
126.878–135.159	2.0	0.081	119
142.558–150.838	2.1	0.081	119
218.070–225.850	45.7	0.317	702
IRAM 30 m, frequency switching			
87.064–94.844	2.8–3.6	0.052–0.101	140–158
143.055–150.838	3.6–5.0	0.106–0.262	170–232

Notes. [a]The rms level depends on the time of integration and was different for each source and frequency band, e.g., the best APEX result was achieved for NGC 1333-IRAS 2A (position 1) with a 171 min integration time at 219 GHz with an rms of 7.8 mK. The best IRAM rms (=2.0 mK) level was reached for L1551-IRS 5 for the HOOH transition at 131.396 GHz with an integration time of 325 min.

single-sideband (SBB) front-ends combined with the fast Fourier transform spectrometer XFFTS2 as spectral back-end with a 2500 MHz bandwidth per input (four inputs). All APEX measurements were made in position-switching mode, or more precisely, in its variant as wobbler switching (wobbler throw of 60″), where only the subreflector is moved instead of the entire telescope. We checked the pointing and focus every ~1.5 and ≤4 h, respectively.

The observations using the IRAM 30 m telescope at the Pico del Veleta in Spain toward L1551-IRS 5 and L1544 were made during three consecutive nights in August 2016 (August 24 to 26)[2]. On the first night, L1551 was investigated in position-switching mode at 83.9–91.7 GHz, 126.9–135.2 GHz, 142.6–150.8 GHz, and 218.1–225.9 GHz using the heterodyne Eight MIxer Receiver (EMIR) at 3 mm (E090), 2 mm (E150), and 1.3 mm (E230) wavelengths in SSB mode (Carter et al. 2012). Two polarizations, vertical and horizontal, were recorded simultaneously. As back-end the fast Fourier transform spectrometer (FTS200) with a 200 kHz resolution and 7.78 GHz bandwidth per sideband was used[3]. During the subsequent two nights, L1551 and L1544 were investigated using the frequency-switching mode at 87.1–94.8 GHz and 143.1–150.8 GHz. The weather conditions were favorable during most of the time, as were the overall system conditions; see Table 2. The total on-source time at IRAM 30 m was 17.6 h.

The basic data reduction and processing was made using the continuum and line analysis single-dish software (CLASS) from the GILDAS[4] software package. As a standard procedure, we checked the quality of the scans and eliminated bad channels.

Then we made baseline corrections with a subsequent averaging over individual scans. We identified molecular line positions and used a Gaussian line shape or a superposition of Gaussian line shapes[5] to extract their velocity-integrated intensities W^* and line widths (full width at half-maximum, FWHM).

Because for both telescopes the output spectra are provided as calibrated antenna temperatures (T_{A}^*), the brightness temperature T_{B} has to be calculated according to the telescope in use, for example, through the main beam temperature T_{mb} (see Velilla-Prieto et al. (2017) for a similar approach),

$$T_{\text{B}} = T_{\text{mb}}\, \text{bff}^{-1} = T_{\text{A}}^*\, \eta^{-1}\, \text{bff}^{-1} \tag{1}$$

with $\eta^{-1} = F_{\text{eff}}/B_{\text{eff}}$ and $\text{bff}^{-1} = (\theta_{\text{b}}^2 + \theta_{\text{s}}^2)/\theta_{\text{s}}^2$. (2)

Here, bff is the beam-filling factor, B_{eff} is the main-beam efficiency of the antenna, F_{eff} is the forward efficiency of the antenna, θ_{s} is the source size (diameter of the emitting region), and θ_{b} is the half-power beam width (HPBW) of the main beam of the antenna[6]. The HPBW θ_{b} of the antenna main beam can be approximated for each specific telescope using the expression

$$\theta_{\text{b}}('') = a/\nu(\text{GHz}), \tag{3}$$

with $a_{\text{APEX}} = 6091.3\,[\text{GHz}/('')]$ and $a_{\text{IRAM}} = 2446.0\,[\text{GHz}/('')]$. The main-beam efficiency η can be calculated using the approximation (Velilla-Prieto et al. 2017)

$$\eta^{-1} \equiv F_{\text{eff}}/B_{\text{eff}} = b\, \exp{(\nu(\text{GHz})/c)^2}, \tag{4}$$

with $b_{\text{APEX}} = 1.233$ and $c_{\text{APEX}} = 1074.0\,(\text{GHz})$ for the APEX 12 m telescope and $b_{\text{IRAM}} = 1.115$ and $c_{\text{IRAM}} = 399.5\,(\text{GHz})$ for the IRAM 30 m telescope.

4. Data analysis methods

The observations were analyzed using two methods. In method 1 we used the measured integrated intensities W (in [K km s^{-1}]), that is, W^* corrected for and calculated using T_{B} instead of T_{A}^*, to produce a population diagram (also known as Boltzmann plot or rotational diagram) of each detected molecule. By assuming local thermodynamic equilibrium (LTE) conditions, we were able to extract the respective total column density N_C and rotational temperature T_{rot} of the molecule under investigation. The equation we used is similar to the one used in Goldsmith & Langer (1999) and Velilla-Prieto et al. (2017) and is given by

$$\ln\left(\frac{N_{\text{u}}}{g_{\text{u}}}\right) = \ln\left(\frac{3k_{\text{B}}W}{8\pi^3\nu\, S_{\text{ul}}\mu^2}\right) = \ln\left(\frac{N_{\text{C}}}{Q}\right) - \frac{E_{\text{u}}}{k_{\text{B}}T_{\text{rot}}}, \tag{5}$$

with N_{u} the column density of the upper level, g_{u} the degeneracy of the upper level, k_{B} the Boltzmann constant, ν the rest frequency of the molecule transition, S the line strength, μ the dipole moment of the molecule, Q the partition function, and E_{u} the upper energy level of this transition. For many astrophysically relevant molecules, the information needed (ν, S_{ul}, μ, Q and E_{u}) is provided in databases such as the Cologne Database

---

Table 3. Observational results at HOOH transition frequencies.

Obs. frequency (MHz)	Beam size (")	rms (mK)	$FWHM^{(a)}$ (expect.) (km s^{-1})	$\int T_{mb} dv$ (mK km s^{-1})
R CrA -IRS 5A				
219 166.8600	27.8	9.7(4)	0.7–1.4	<6.8–13.6
251 914.6794	24.2	23.7	0.7–1.4	<16.6–33.2
318 222.5200	19.1	38.6	0.7–1.4	<27.0–54.0
318 712.1000	19.1	34.5	0.7–1.4	<24.2–48.3
NGC 1333-IRAS 2A-1 (center position/position 1)$^{(*)}$				
219 166.8600	27.8	8.0	0.66–2.7$^{(b)}$	<5.3–21.6
318 222.5200	19.1	43.2	same$^{(c)}$	<28.5–116.6
318 712.1000	19.1	40.6	same$^{(c)}$	<26.8–109.6
L1551-IRS 5				
90 365.5097	26.8	6.6	1.4–2.5	<9.9–16.5
143 712.6282	21.7	2.1	1.4–2.5	<3.2–5.3
219 166.8600	14.6	45.4	1.4–2.5	<63.6–113.5
L1544				
90 365.5097	26.8	2.8	0.6–1.8	<1.7–5
143 712.6282	21.7	5.0	0.4–0.9	<2–4.5

Notes. $^{(a)}$Expected line width inferred from line widths of other molecules (H$_2$CO, CH$_3$OH, etc.) in the same source. $^{(b)}$Inferred from H$_2$CO line at 218.22 GHz. The HOOH line width is most likely around 1.5 km s^{-1}. $^{(c)}$Because no line could be detected in the full spectral range of 318 GHz, the line width was adopted from the 219 GHz value. $^{(*)}$No detectable line on NGC 1333-IRAS 2A positions 2 and 3.

for Molecular Spectroscopy (CDMS)[7], or the Jet Propulsion Laboratory (JPL) molecular lines catalog[8]. References to the original spectroscopic literature can be found there as well.

The second method uses the eXtended CASA Line Analysis Software Suite (XCLASS)[9] by Möller et al. (2017). XCLASS is a supplementing software for the Common Astronomy Software Applications package (CASA; McMullin et al. 2007) and also works well with python[10] -based software. From this software package we mainly used the myXCLASS program to model our data. This program models a spectrum by solving the radiative transfer equation for an isothermal object (Stahl & Palla 2005). Similar to the aforementioned method, myXCLASS assumes LTE, meaning that per molecule only one excitation temperature is assumed for all transitions[11]. From the input spectrum the program calculates the temperature as well as the column density N_C of the molecule. Thus, both methods give quantities that can be directly compared with each other.

5. Observational results

We focused on the analysis of HOOH[12] toward the objects described above, and the observational results are listed in Table 3. Other molecular lines that we observed in these sources

---

[7] See https://cdms.astro.uni-koeln.de/, Endres et al. (2016).
[8] See https://spec.jpl.nasa.gov/, Pickett et al. (1998).
[9] See https://xclass.astro.uni-koeln.de/
[10] Python Software Foundation, https://www.python.org/
[11] CLASS can separate between several emitting regions (core layers) with different excitations temperatures, velocity offsets, etc. However, we only used one core layer to analyze the data.
[12] The spectroscopic data of HOOH are based on Petkie et al. (1995) and Camy-Peyret et al. (1992).

in the mentioned frequency ranges are not discussed further. In R CrA-IRS 5A, for instance, we identified ^{13}CO, SO, NO, c-C$_3$H$_2$, CN isotopologs, DCN, and HCCNC. The molecules H$_2$CO and CH$_3$OH are discussed in another study, together with detailed information on the model (Fuchs et al. 2020).

According to the model temperatures in the sources (see Table 4), and the specifications of the telescopes, we focused our observations on the 219.2 GHz line for R CrA-IRS 5A and NGC 1333-IRAS 2A using the APEX 12 m telescope and the 143.7 GHz line for L1551-IRS 5 and L1544 using the IRAM 30 m telescope. In the following paragraphs the observations for each source will be discussed in detail. We show below that HOOH is not clearly detected in any of the investigated sources. Instead, only upper limits for HOOH column densities can be derived for the individual sources, defined by their respective rms levels. In Table 3 a list of all targeted HOOH frequency positions is given, including the integrated line intensities at these positions. Table A.1 shows a list of relevant HOOH transitions, including spectroscopically relevant parameters used in Eq. (5)[13].

R CrA-IRS 5A. As an example, the R CrA-IRS 5A observation is shown in Fig. 1. Here, the 219.2 GHz region was observed using 1008 scans, resulting in 150 min integration time and an rms level of 9.7 mK. As an example, a simulated line profile with an FWHM of 1.4 km s^{-1} is included at the expected HOOH frequency position close to 219.2 GHz. With the analysis methods we described above (Sect. 4), the integrated line intensity can be used to infer an upper limit of about 6–9 × 10^{11} cm^{-2} (see Table 4). This result is not very sensitive to the assumed temperature, that is, between 13 and 25 Kelvin. The upper limit is also consistent with other observed frequency regions, as we verified using the myXClass program.

Spectra at HOOH line positions for the other sources, that is, for NGC 1333-IRAS 2A, L1551-IRS 5, and L1544, can be found in the Appendix section (Figs. A.1–A.3). Below we only summarize the conclusions.

NGC 1333-IRAS 2A. This source was investigated at three spatial positions (see Table 1). The line analysis for this source is not as straightforward as for the calm source close to R CrA. For the center position (position 1), the line profile may be different from the assumed Gaussian line shape, as can be observed for the H$_2$CO lines (not shown here, see Fuchs et al. 2020), which are more similar to P Cygni profiles. Despite the long integration time of 171 min for position 1 and 119 min for position 3, HOOH is not detected at any of the frequency settings; see Fig. A.1. Assuming a temperature of around 22 K results in an upper limit for the HOOH column density toward position 1 of about 2–7 × 10^{11} cm^{-2}.

*L1551-IRS 5.* Although we used a large telescope (30 m dish) and very long integration times (325 min in position-switching mode), which allowed us to see an rms level of only 2.1 mK at 143 GHz, no signal at the HOOH $(4_{1,3}-3_{0,3})$ frequency position could be detected; see Fig. A.2. Similar to NGC 1333-IRAS 2A, the expected line profile is more complicated because of the influence of a molecular outflow (see H$_2$CO and CH$_3$OH spectra in Fuchs et al. 2020). The source was

---

[13] $S\mu^2$ can be calculated by converting the intensity I [nm^{2}MHz] at a given temperature T using $S_g\mu_g^2 = 2.40251 \times 10^4 I(T) Q_{rs}(T) \nu^{-1} (e^{-E''/kT} - e^{-E'/kT})^{-1}$, see Pickett et al. (1998). The partition function values $Q(T)$ were calculated using the tables given in the CDMS and JPL catalogs.

Table 4. Comparison between the gradient model predictions for HOOH and observational results (rotational diagram method and myXClass).

| Source | Gradient model | | | Observational results | | | |
| | HOOH | | | Rotational diagram | | myXClass | |
	emission region (")	aver. T [*] (K)	N_T(HOOH) [*] (cm^{-2})	T_{rot} (K)	N_T(HOOH) [**] upper limits (cm^{-2})	T_{ex} (K)	N_T(HOOH) upper limits (cm^{-2})
R CrA-IRS 5A	64.5	21(4)	$5(5) \times 10^{12}$	21.4 [a]	$\leq 5.8(20) \times 10^{11}$ [a]	13–25	$\leq 8.8(2) \times 10^{11}$
NGC 1333-IRAS 2A-1	66.6	22(4)	$10^{13.2} - 10^{16.4}$	21.5 [b]	$\leq 6.9(56) \times 10^{11}$ [b]	22^{fixed}	$\leq 2.7(5) \times 10^{11}$
L1551-IRS 5	91.8	21(4)	$9(9) \times 10^{12}$	21.4 [c]	$\leq 1.6 \times 10^{11}$ [c]	17–25	$\leq 2.2 \times 10^{11}$
L1544	114.3	12.5 [d]	$10^{11.7} - 10^{14.6}$	12.5 [d]	$\leq 1.9(45) \times 10^{11}$ [e]	12.5^{fixed}	$\leq 1.9 \times 10^{11}$

Notes. [*] The indicated uncertainties are mainly due to age uncertainties of the sources and the boundary conditions of the chosen integration limits (inner and outer shell radii). Early sources such as NGC 1333-IRAS 2A-1 and L1544 show a high age dependence for HOOH. [**] Column densities were obtained by applying the rotational diagram technique. For HOOH, the observational upper limit is determined using the average and broader line width values from Table 3. [a] A temperature of 21.4 K (model value) was assumed. However, the value of the column density is not very temperature sensitive, i.e., assuming $T = 25$ K results in nearly the same N_T. [b] Assuming an expected line width of 1.5 km s^{-1}. The 219 GHz rms level was used. Fitted assuming $T = 21.5$ K (model value). [c] Assuming a temperature at 21.4 K (model value). The 143 GHz rms was used (because of the longest integration time). [d] Temperature taken from Tafalla et al. (1998). [e] Assuming a temperature at 12.5 K (Tafalla et al. 1998) and using the 143 GHz rms level.
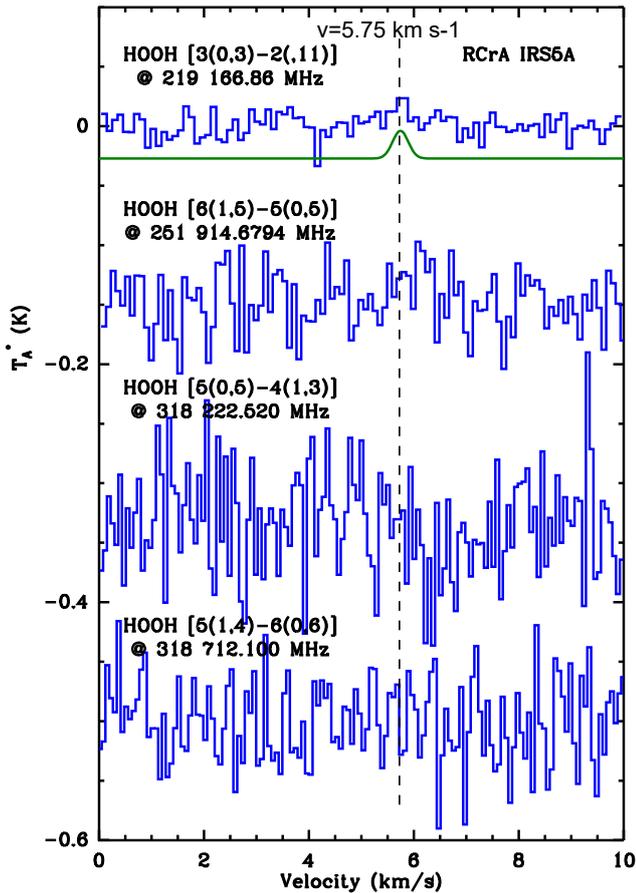
Fig. 1. Region with HOOH transitions toward R CrA-IRS 5A. The green line indicates the HOOH line position. Its line intensity is consistent with the rms level. All spectra have the same intensity scale, but (except for the first) are plotted with an intensity offset.

observed in position- and frequency-switching mode (400 min; 3.6 mK rms level) at 143 GHz. Using the model temperature of 21 K, we determined the upper limit for the HOOH column density as about 2×10^{11} cm^{-2}.

L1544. Generally, this source reveals narrow lines that can be easily fit using a Gaussian line profile. The deconvolved spectra taken in a frequency-switching mode are shown in Fig. A.3. Assuming a temperature of 12.5 K (Tafalla et al. 1998), we determine the upper limit for the HOOH column density as 2×10^{11} cm^{-2}.

In conclusion, our study yields a set of upper column density values for HOOH that span 2–9×10^{11} cm^{-2} for the investigated sources.

6. Comparison with model data

The results of the observations are summarized and compared to the predicted values by our gradient model in Table 4. The modeled water vapor results are not mentioned in this table because we do not have any observations of H_2O transitions, but the water abundances are discussed below and are compared with results from other groups. In none of the four investigated sources were we able to identify hydrogen peroxide signals, and the estimated column densities are expected to be below the derived upper limit values that roughly cover 2–9×10^{11} cm^{-2}. These nondetections of HOOH in protostellar environments are unfortunate, but agree with a number of previous studies in which this molecule could not be detected either.

R CrA-IRS 5A (Class 1). This source proved to be well suited for our applied gradient model. The spectra are not dominated by internal source dynamics, such as outflows, and allow a straightforward analysis. With a relative [HOOH]/[H_2] abundance of 5×10^{-10}, the model predicted an HOOH abundance nearly an order of magnitude higher than what we derived as upper limit from the observations. Geometry aspects, that is, the assumed density and temperature gradient of the YSO, are most likely not the cause for this discrepancy (Fuchs et al. 2020). Our modeled gas-phase water abundance is $X = [H_2O]/[H_2] = 2 \times 10^{-8}$ and agrees with the $X \approx 10^{-8}$ deduced by Schmalzl et al. (2014). In our model the solid HOOH abundance is indicative for the H_2O production and seems to fit to the latter number. However, the calculated gas-phase HOOH abundance is clearly too high. Although we see no fundamental contradiction between

a good agreement of the model and observational values for gas-phase H_2O, the nondetection of HOOH is therefore still surprising in view of the fact that H_2O abundances (and the abundance of other molecules[14]) can be well described by the model.

NGC 1333-IRAS 2A (Class 0). Because of the inner structure and dynamics, the deviation between the modeled structure of the object and the observed geometry is stronger than in the other investigated sources. To compare the observations with the model, certain assumptions (such as the restriction to the $v_{lsr} = 7.34$ km s^{-1} component of the multipeak molecular transition lines) had to be made. Furthermore, this source is very young, which causes the model to produce unrealistically high HOOH column densities. Consequently, the predicted HOOH abundances ([HOOH]/[H_2] $\approx 7 \times 10^{-10}$–$10^{-6}$) could not be confirmed and only an upper limit could be given. In case of water vapor, our model results in a relative abundance of [H_2O]/[H_2] $\approx 3 \times 10^{-8}$–6×10^{-7} depending on the age of the source, with the lower value corresponding to a more evolved source ($\approx 10^5$ yr). Observations by Kristensen et al. (2012) indicate a relative water abundance of $\approx 10^{-8}$. However, according to the same authors, the source is a young Class 0 object ($\sim 2 \times 10^4$ yr). No conclusive result can therefore be drawn, but given the long integration times at the APEX 12 m telescope, further single-dish searches for this molecule toward IRAS 2A will most likely not result in a detection.

L1551-IRS 5 (Class 1). Similar to NGC 1333-IRAS 2A, the spectra reveal dynamical and most likely non-LTE processes within this source. In our analysis we focused on the narrow $v_{lsr} = 7.0$ km s^{-1} component of the lines. In our model the column density of water vapor is 3.4×10^{14} cm^{-2} and very close to the observed 3.1×10^{14} cm^{-2} by Schmalzl et al. (2014)[15]. Concerning the HOOH molecule, the column density of about 1×10^{13} cm^{-2} predicted by our model could not be confirmed by the observations. The corresponding relative [HOOH]/[H_2] abundance is 3×10^{-8}. The new observationally determined upper limit is about 40 times lower than this value when a temperature between 17 and 25 K is assumed. Like in the other Class 1 source, that is, R CrA-IRS 5A, the model overestimates the HOOH abundance but produces fairly good predictions for other investigated molecules.

L1544 (prestellar core). Previous work by Tafalla et al. (1998) suggested that molecules can be seen in this source at low temperatures. In our model we assumed a 12.5 K temperature for HOOH. The upper abundance limit of this molecule is lower than the predicted value (even below the lower value given in Table 4), which is indicative of the already known weakness of the model, which tends to overestimate HOOH at early stages. The calculated relative [HOOH]/[H_2] abundance is 2×10^{-12}–2×10^{-9} depending on the age of the source. When the relative water vapor abundance is calculated, our gradient model results ($X_{H_2O} = 10^{-8}$–10^{-9}) disagree with estimated abundances from observations ($<1.4 \times 10^{-10}$) by Caselli et al. (2012). Because of the low temperatures, Caselli et al. (2012) were surprised to observe water vapor emission in its inner core. Our hope that this somewhat unexpected detection might be based on mechanisms that also drive HOOH into the gas phase has not been fulfilled.

---

[14] See H_2CO and CH_3OH abundances in Fuchs et al. (2020).
[15] We used a $N_{hydrogen}$ column density of 1.2×10^{22} cm^{-2}, whereas Schmalzl et al. (2014) used $N_H = 7.4 \times 10^{23}$ cm^{-2}, resulting in a relative H_2O abundance of 4×10^{-10}.

Table 5. Sources in which HOOH has been searched for.

Source	HOOH rms (mK)	HOOH $\int T_{mb} dv$ (mK km s^{-1})	Ref.
ρ Oph-A		167 [a]	[1]
Orion "H_2-Peak 1"	26.1 [b]	172 [b]	[2]
r Oph-B2-MM8	22.9		[3]
G15.01-0.67	19.2		[3]
G018.82-00.28MM1	21.1		[3]
G018.82-00.28MM4	21.0		[3]
G028.53-00.25MM1	17.7		[3]
NGC 6334I(N)	18.6		[3]
G1.6-0.025	16.1		[3]
NGC 1333-IRAS 4A	24.6		[3]
L1527	18.4		[3]
R CrA-IRS 7B	23.1		[3]
IRAS 16293-2422	<67		[4]
R CrA-IRS 5A	9.7 [a]	≤10.2 [a]	[5]
NGC 1333-IRAS 2A	8.0 [a]	≤13.5 [a]	[5]
L1551-IRS 5	2.1 [c]	≤4.3 [c]	[5]
L1544	5.0 [c]	≤4.5 [c],[d]	[5]

Notes. [a]Transition $3_{0,3}$–$2_{1,1}$ at 219.167 GHz; [b]value from transition $3_{0,3}$–$2_{1,1}$ at 219.167 GHz, which is one of five observed HOOH transitions, with the best S/N. Here the integrated area is given in $\int T_A dv$ and not in $\int T_{mb} dv$; [c]value from transition $4_{1,3}$–$3_{0,3}$ at 143.712 GHz; [d]instead of using the mean FWHM value in Table 3, we assumed the higher FWHM value to estimate the upper limit.

References. [1] Bergman et al. (2011a), [2] Liseau & Larsson (2015), [3] Parise et al. (2014), [4] TIMASS survey Caux et al. (2011), and [5] this work.

7. Discussion

So far, HOOH has been identified in only two sources, one of which (OMC-1) is still not fully verified; see Table 5. Coincidentally, these sources are the only ones in which the precursor molecule oxygen (O$_2$) could be identified[16], but with very low O$_2$/H$_2$ ratios, for example, O$_2$/H$_2$ $\approx$ 5×10^{-8} in ρ Oph A (Liseau et al. 2012).

Both sources are in regions where nearby stars cause high irradiation. New investigations of the radiation field at ρ Oph A (Lindberg et al. 2017) indicate, for example, that the H_2CO rotational temperatures in the protostellar envelopes of this region are strongly enhanced close to the Herbig Be star S1 (similarly, see also the study by Lindberg et al. (2015) for the CrA star-forming region). Lindberg et al. (2017) write that "for some reason, the H_2CO gas is more prone to be heated by external radiation fields, or the H_2CO abundance is enhanced in the irradiated gas, possibly due to photochemistry". The role of an external radiation field has yet not been properly investigated for HOOH. For example, it might well be that the chemistry is changed or that desorption is enhanced. In the case of water, it is known that photodesorption takes place, but that dissociative reactions on the surface also take place, that is, the transition grain-gas can be destructive and thus decrease the water gas-phase abundance (Anderson & van Dishoeck 2008; Öberg et al. 2009).

---

[16] See Larsson et al. (2007); Liseau et al. (2012); Goldsmith et al. (2011) and Chen et al. (2014).

Our model can be applied to a flat geometry and reproduces the HOOH abundance toward ρ Oph A without explicitly taking these effects into account (e.g., the desorption rate results mainly from the exothermal energy during the HOOH formation, not from radiation). This might be due to these as yet unknown or very difficult to model effects that are missing or misinterpreted in our chemical model and lead to incorrect results for the sources we investigated here. To further investigate the interplay of radiation with HOOH formation and photodesorption, we are currently bound to the two sources ρ Oph A and Orion A. However, a model refinement can only be successful if more data are available, either in the form of higher spacial resolution of the molecule distribution of HOOH and related grain-borne molecules, or as an increased set of observed molecular species to obtain a better picture of the local radiation fields[17].

Evidence of HOOH in one or two sources, and the nondetection of HOOH in many investigated objects, may be interesting in connection with the chemistry of our own Solar System. Has our primordial solar environment been special? Measurements by the double-focusing mass spectrometer (DFMS) of the Rosetta Orbiter Spectrometer for Ion and Neutral Analysis (ROSINA) of the coma of comet 67P/Churyumov-Gerasimenko (Bieler et al. 2015) indicate abundant molecular oxygen and reveal an hydrogen peroxide to oxygen ratio of $[H_2O_2]/[O_2] = (0.6 \pm 0.07) \times 10^{-3}$ which is very close to the ratio measured in the ρ Ophiuchi dense core $[HO_2]/[O_2] < [H_2O_2]/[O_2] < 0.6 \cdot 10^{-3}$ (Bergman et al. 2011a; Parise et al. 2012). Bieler et al. (2015) argued that if these gas-phase abundance ratios reflect those in the cometary ice, it would support the existence of primordial O_2. Furthermore, the ρ Ophiuchi A core has been suggested to have a higher temperature, that is, about 20–30 K, compared to 10 K for most other dense interstellar clouds, which is also typical of estimates for the comet-forming conditions in the outer early solar nebula. This would suggest that our Solar System might have formed from an unusually warm molecular cloud. However, Luspay-Kuti et al. (2018) pointed out that O_2 condensation in the protosolar nebula might not be the only cause of the measured abundances, but that also in situ O_2 formation processes (e.g., post-accretion radiolysis) might be at play that connect this molecule with H_2O and related molecules such as hydrogen peroxide (e.g., O_2 formation via HOOH dismutation or disproportionation).

8. Conclusions

At the heart of this work is the attempt to answer the question whether it can be shown that water is formed on grain surfaces through a chemical pathway that includes hydrogen peroxide as the main intermediate. For this we searched for HOOH gas-phase signatures exclusively in the dense environments of YSOs and in a prestellar core and assumed that HOOH can be released into the gas phase, thermally or through other means, after it has formed in the solid state. A model that combines a previously used chemical model (Du et al. 2012) and a physical model that takes into account the shell-like structure of typical protostellar objects was used for this purpose (see "gradient model" in Fuchs et al. 2020). Based on predictions by this model, four sources were chosen in which an HOOH detection seemed feasible and in which water has previously been detected. Despite long integration times on the APEX 12 m and IRAM 30 m telescopes, we cannot report an unambiguous hydrogen peroxide

detection for any of these targets. Further support for an H_2O solid-state formation scheme through HOOH, that is, by comparing relative abundances, is therefore not possible. However, this nondetection does not exclude the proposed solid-state formation scheme. As said in the introduction, as an intermediate, HOOH may fully react to water, resulting in rather low ice and also gas-phase HOOH abundances. It is also possible that reactive desorption as a possible sublimation process is not efficient enough to build up substantial HOOH gas-phase abundances, and it is equally well possible that HOOH, after it is released from the ice, forms the starting point in a gas-phase reaction. At this stage, it is not clear how other not yet included chemical reaction mechanisms, both in the solid state and in the gas phase, will affect the abundance of HOOH. For this, follow-up studies are required. Another promising development that helps to investigate the surface-reaction scheme would be a direct solid-state detection of HOOH in the infrared region, similar to those available for H_2O ice, or other ice-borne molecules such as H_2CO and CH_3OH. This will not be straightforward because only a broad HOOH band around 1400–1500 cm^{-1} is clearly different from H_2O vibrational modes. Unfortunately, vibrational modes from other abundant species can also be found in this region. Our hope is that new insights will arise from dedicated ice surveys performed by the *James Webb* Space Telescope (JWST) in the near future.

References

Ainsworth, R. E., Coughlan, C. P., Green, D. A., Scaife, A. M. M., & Ray, T. P. 2016, MNRAS, 462, 2904
Andersson, S., & van Dishoeck, E. F. 2008, A&A, 491, 907
Bergman, P., Parise, B., Liseau, R., et al. 2011a, A&A, 531, L8
Bergman, P., Parise, B., Liseau, R., & Larsson, B. 2011b, A&A, 527, A39
Bieler, A., Altwegg, K., Balsiger, H., et al. 2015, Nature, 526, 678
Bizzocchi, L., Caselli, P., Spezzano, S., & Leonardo, E. 2014, A&A, 569, A27
Bottinelli, S., Ceccarelli, C., Williams, J. P., & Lefloch, B. 2007, A&A, 463, 601
Boudin, N., Schutte, W. A., & Greenberg, J. M. 1998, A&A, 331, 749
Brinch, C., Jorgensen, J. K., & Hogerheijde, M. R. 2009, A&A, 502, 199
Camy-Peyret, C., Flaud, J.-M., Johns, J. W. C., & Noël, M. 1992, J. Mol. Spect., 155, 84
Carter, M., Lazareff, B., Maier, D., et al. 2012, A&A, 538, A89
Caselli, P., Walmsley, C. M., Zucconi, A., et al. 2002, ApJ, 565, 344
Caselli, P., Keto, E., Bergin, E. A., et al. 2012, ApJ, 759, L37
Caux, E., Kahane, C., Castets, A., et al. 2011, A&A, 532, A23
Cazaux, S., Minissale, M., Dulieu, F., & Hocuk, S. 2016, A&A, 585, A55
Chen, W. P., & Graham, J. A. 1993, ApJ, 409, 319
Chen, J.-H., Goldsmith, P. F., Viti, S., et al. 2014, ApJ, 793, 111
Cuppen, H. M., Ioppolo, S., & Linnartz, H. 2010, Phys. Chem. Chem. Phys., 12, 12077
Crapsi, A., Caselli, P., Walmsley, C. M., et al. 2005, ApJ, 619, 379
Crapsi, A., Caselli, P., Walmsley, M. C., & Tafalla, M. 2007, A&A, 470, 221
Du, F., Parise, B., & Bergman, P. 2012, A&A, 538, A91
Dulieu, F., Amiaud, L., Congiu, E., et al. 2010, A&A, 512, A30
Endres, C. P., Schlemmer, S., Schilke, P., et al. 2016, J. Mol. Spectr., 327, 95
Engargiola, G., & Plambeck, R. L. 1999, The Physics and Chemistry of the Interstellar Medium, eds.: V. Ossenkopf, J. Stutzki, & G. Winnewisser (Cambridge: Cambridge University Press)
Franklin, J., Snell, R. L., Kaufman, M. J., et al. 2008, ApJ, 674, 1015
Fuchs, G. W., Witsch, D., Herberth, D., et al. 2020, A&A, submitted
Goldsmith, P. F., & Langer, W. D. 1999, ApJ, 517, 209
Goldsmith, P. F., Melnick, G. J., Bergin, E. A., et al. 2000, ApJ, 539, L123
Goldsmith, P .F., Liseau, R., Bell, T. A., et al. 2011, ApJ, 737, 96
Güsten, R., Nyman, L. Å., Schilke, P., et al. 2006, A&A, 454, L13
Hollenbach, D., Kaufman, M. J., Bergin, E. A., & Melnick, G. J. 2009, ApJ, 690, 1497
Hunt, R. H., Leacock, R. A., Peters, C. W., & Hecht, K. T. 1965, J. Chem. Phys., 42, 1931

[17] With the recent work by Larsson et al. (2017), more data on ρ Oph A are now available to further investigate these questions.

Ioppolo, S., Cuppen, H. M., Romanzin, C., et al. 2008, ApJ, 686, 1474

Ioppolo, S., Cuppen, H. M., Romanzin, C., et al. 2010, Phys. Chem. Chem. Phys., 12, 12077

Ivezic, Z., & Elitzur, M. 1997, MNRAS, 287, 799

Jørgensen, J. K., Hogerheijde, M. R., van Dishoeck, E. F., et al. 2004a, A&A, 413, 993

Jørgensen, J. K., Hogerheijde, M. R., Blake, G.A., et al. 2004b, A&A, 415, 1021

Kristensen, L. E., van Dishoeck, E. F., van Kempen, T. A., et al. 2010, A&A, 516, A57

Kristensen, L. E., van Dishoeck, E. F., Bergin, E. A., et al. 2012, A&A, 542, A8

Larsson, B., & Liseau, R. 2017, A&A, 608, A133

Larsson, B., Liseau, R., Pagani, L., et al. 2007, A&A, 466, 999

Lee, J.-E., Lee, J., Lee, S., et al. 2014, ApJS, 214, 21

Lefloch, B., Cabrit, S., Codella, C., et al. 2010, A&A, 518, L113

Lindberg, J. E., Jørgensen, J. K., Watanabe, Y., et al. 2015, A&A, 584, A28

Lindberg, J. E., Charnley, S. B., Jørgensen, J. K., et al. 2017, ApJ, 835, 3

Liseau, R., & Larsson, B. 2015, A&A, 583, A53

Liseau, R., Goldsmith, P. F., Larsson, B., et al. 2012, A&A, 541, A73

Luspay-Kuti, A., Mousis, O., Lunine, J. I., et al. 2018, Space Sci. Rev., 214, 115

McMullin, J. P., Waters, B., Schiebel, D., et al. 2007, ASP Conf. Ser., 376, 127

Melnick, G. J., & Bergin, E. A. 2005, Adv. Space Res., 36, 1027

Miyauchi, N., Hidaka, H., Chigai, T., et al. 2008, Chem. Phys. Lett., 456, 27

Mottram, J. C., Kristensen, L. E., van Dishoeck, E. F., et al. 2014, A&A, 572, A21

Minissale, M., Dulieu, F., Cazaux, S., & Hocuk, S. 2016, A&A, 585, A24

Möller, T., Endres, C., & Schilke, P. 2017, A&A, 598, A7

Nisini, B., Antoniucci, S., Giannini, T., & Lorenzetti, D. 2005, A&A, 429, 543

Nutter, D. J., Ward-Thompson, D., & Andre, P. 2005, MNRAS, 357, 975

Oba, Y., Miyauchi, N., Hidaka, H., et al. 2009, ApJ, 701, 464

Öberg, K. I., Linnartz, H., Visser, R., & van Dishoeck, E. F. 2009, ApJ, 693, 1209

Osorio, M., D'Alessio, P., Muzerolle, J., et al. 2003, ApJ, 586, 1148

Parise, B., Bergman, P., & Du, F. 2012, A&A, 541, L11

Parise, B., Bergman P., & Menten, K. 2014, Faraday Discuss., 168, 349

Peterson, D. E., Caratti o Garatti, A., Bourke, T. L., et al. 2011, ApJS, 194, 43

Petkie, D. T., Goyette, T. M., Holton, J. J., et al. 1995, J. Mol. Spect., 171, 145

Pickett, H. M., Poynter, R. L., Cohen, E. A., et al. 1998, J. Quant. Spectr. Rad. Transf., 60, 883-890

Romanzin, C., Ioppolo, S., Cuppen, H. M., et al. 2011, J. Chem. Phys., 134, 084504

Sandell, G., Knee, L. B. G., Aspin, C., et al. 1994, A&A, 285, L1

Schmalzl, M., Visser, R., Walsh, C., et al. 2014, A&A, 572, A81

Schöier, F. L., Jørgensen, J. K., van Dishoeck, E. F., & Blake, G. A. 2002, A&A, 390, 1001

Shirley, Y. L., Evans II, N. J., Rawlings, J. M. C., & Gregersen, E. M. 2000, ApJS, 131, 249

Smith, R. G., Charnley, S. B., Pendleton, Y. J., et al. 2011, ApJ, 743, 131

Stahler, S. W., & Palla, F. 2005, The Formation of Stars (Weinheim, Germany: Wiley-VCH)

Tafalla, M., Mardones, D., Myers, P. C., et al. 1998, ApJ, 504, 900

Taylor, K. N. R., & Storey, J. W. V. 1984, MNRAS, 209, 5

Tielens, A. G. G. M. 2000, ESA SP, 577, 245

Vandenbussche, B., Ehrenfreund, P., Boogert, A. C. A., et al. 1999, A&A, 346, L57

van Dishoeck, E. F., Kristensen, L. E., Benz, A. O., et al. 2011, PASP, 123, 138

van Dishoeck, E. F., Herbst, E., & Neufeld, D. A. 2013, Chem. Rev., 113, 9043

Velilla Prieto, L., Sánchez Contreras, C., Cernicharo, J., et al. 2017, A&A, 597, A25

Villa, A. M., Trinidad, M. A., de la Fuente, E., & Rodriguez-Esnard, T. 2017, Rev. Mex. Astron. Astrofis., 53, 525

Ward-Thompson, D., Buckley, H. D., Greaves, J. S., et al. 1996, MNRAS, 281, L53

White, G. J., Liseau, R., Men'shchikov, A. B., et al. 2000, A&A, 364, 741

Wilkin, F. P., Chen, H.-R., Chernin, L. M., & Plambeck, R. L. 2002, ArXiv e-prints [arXiv:astro-ph/0212247]

Wirström, E. S., Charnley, S. B., Cordiner, M. A., & Ceccarelli, C. 2016, ApJ, 830, 102

Yıldız, U. A., Acharyya, K., Goldsmith, P. F., et al. 2013, A&A, 558, A58

Appendix A: Tables and figures

**Table A.1.** Relevant transitions of HOOH in the (80–700 GHz) submillimeter region.

| Transition rotational $(J_{K_a,K_c}-J'_{K'_a,K'_c})$	tunneling [†] $\tau' - \tau''$	Frequency (MHz)	log(intensity) at 300K (nm^{2}MHz)	A_{ul} (s^{-1})	E_{up} (K)	Upper state degeneracy $g_{up} = g_I \times g_k$	Spin weight
$3_{1,2}-2_{0,2}$	3–1	*90 365.5097	−4.2979	1.213×10^{-5}	28.2	$7 = 1 \times 7$	1
$4_{1,3}-3_{0,3}$	3–1	*143 712.6282	−3.3341	4.736×10^{-5}	38.1	$21 = 3 \times 7$	3
$5_{1,4}-4_{0,4}$	2–4	197 561.2819	−3.4728	1.205×10^{-4}	50.6	$11 = 1 \times 11$	1
$3_{0,3}-2_{1,1}$	4–2	*219 166.8600	−3.3556	8.584×10^{-5}	31.2	$21 = 3 \times 7$	3
$6_{1,5}-5_{0,5}$	2–4	*251 914.6794	−2.7387	2.458×10^{-4}	65.5	$39 = 3 \times 13$	3
$4_{0,4}-3_{1,2}$	4–2	268 961.1700	−3.4931	1.843×10^{-4}	41.1	$9 = 1 \times 9$	1
$6_{1,5}-7_{0,7}$	3–1	270 610.1000	−2.7781	2.544×10^{-4}	81.9	$39 = 3 \times 13$	3
$5_{0,5}-4_{1,3}$	4–2	*318 222.5200	−2.7632	3.314×10^{-4}	53.4	$33 = 3 \times 11$	3
$5_{1,4}-6_{0,6}$	3–1	*318 712.1000	−3.1657	4.124×10^{-4}	67.0	$11 = 1 \times 11$	1
$3_{1,3}-3_{0,3}$	2–4	616 141.4500	−1.9131	6.762×10^{-3}	44.4	$21 = 3 \times 7$	3
$2_{1,2}-2_{0,2}$	2–4	617 459.1800	−2.5250	6.788×10^{-3}	37.0	$5 = 1 \times 5$	1
$1_{1,1}-1_{0,1}$	2–4	618 341.7600	−2.2622	6.804×10^{-3}	32.2	$9 = 3 \times 3$	3
$1_{1,0}-0_{0,0}$	3–1	670 595.8200	−2.8432	5.786×10^{-3}	32.2	$3 = 1 \times 3$	1

Notes. All values are taken from the JPL catalog; Pickett et al. (1998) (entry: 34 004 H2O2). Frequencies marked with an asterisk are transitions that have been observationally investigated. g_I is the spin-statistical weight, and g_k is the upper state spin-rotational degeneracy (2J+1). [†]Tunneling splitting component (Hunt et al. 1965).
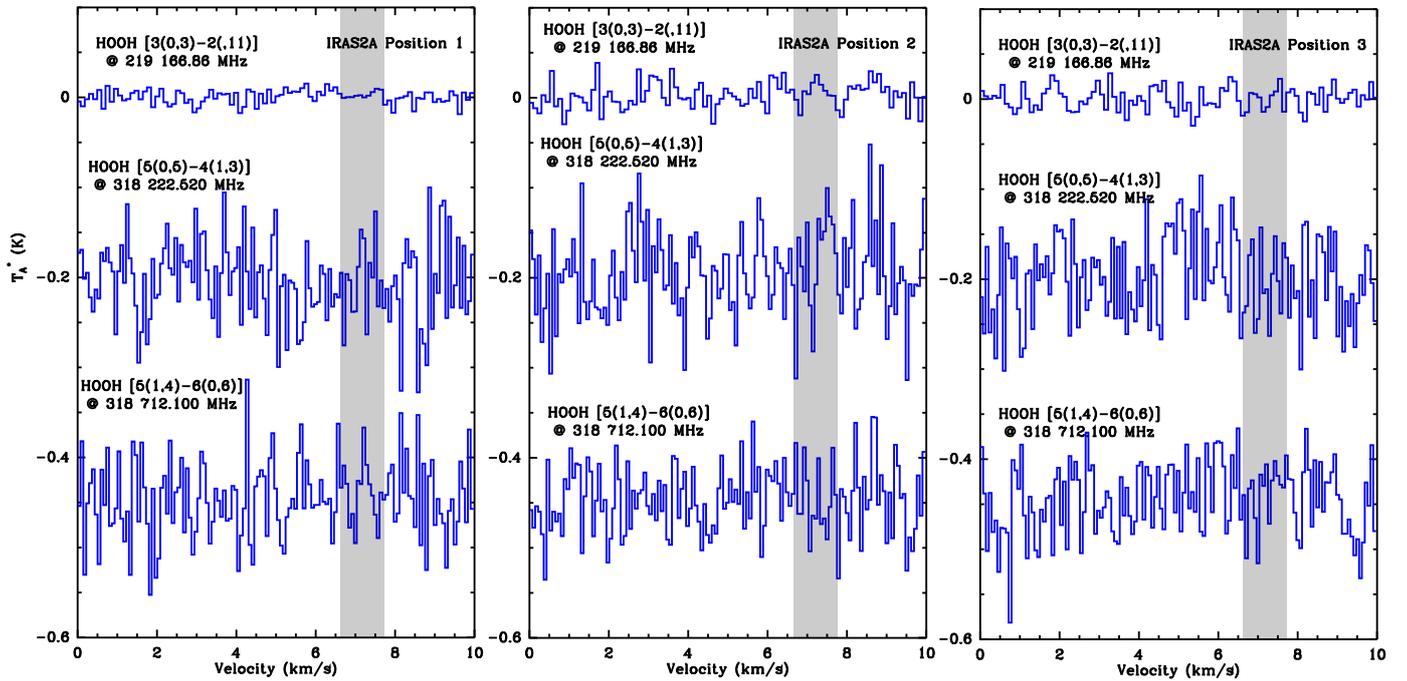
Fig. A.1. Frequency region with HOOH transitions (gray) toward IRAS 2A positions 1–3. All spectra have the same intensity scale, but (except for the top spectra) are plotted with an intensity offset.
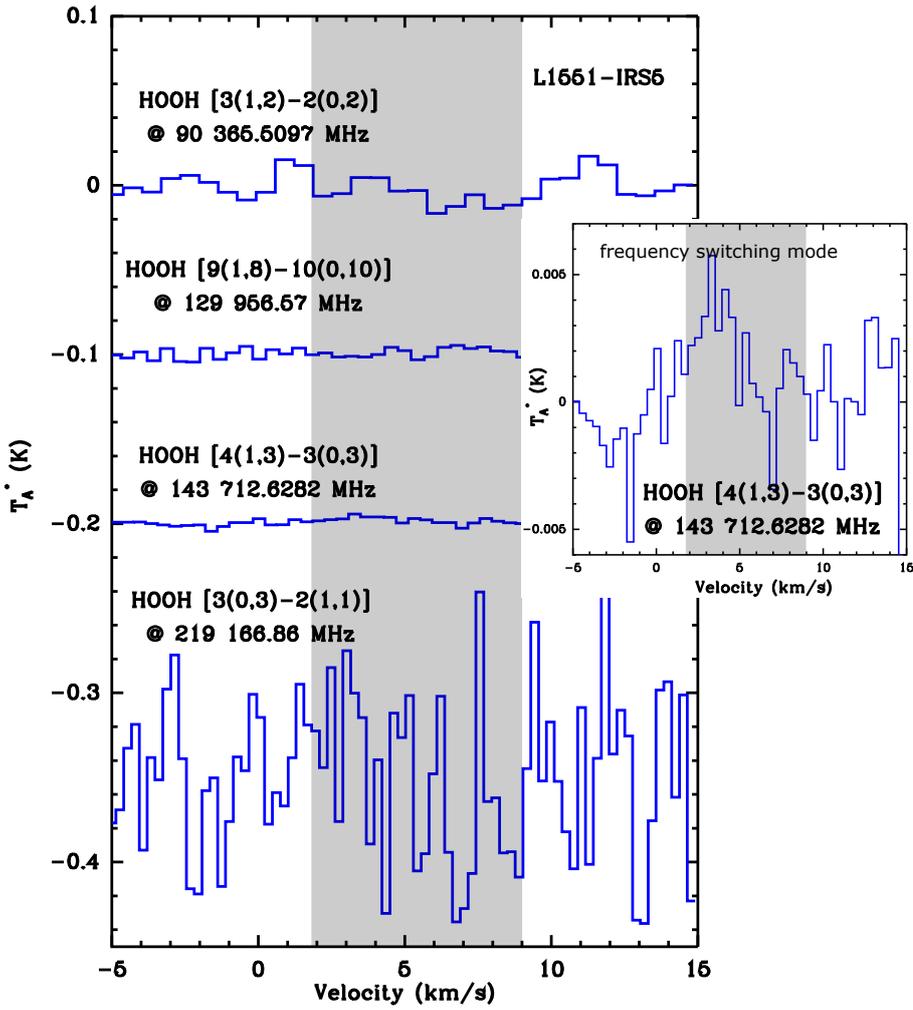
Fig. A.2. Frequency region with HOOH transitions (gray) toward L1551-IRS 5 using position-switching mode. All spectra have the same intensity scale, but (except for the first spectrum) are plotted with an intensity offset. The inset shows the same region around the HOOH transition $4_{1,3}-3_{0,3}$ at 143.71263 GHz using frequency-switching mode.
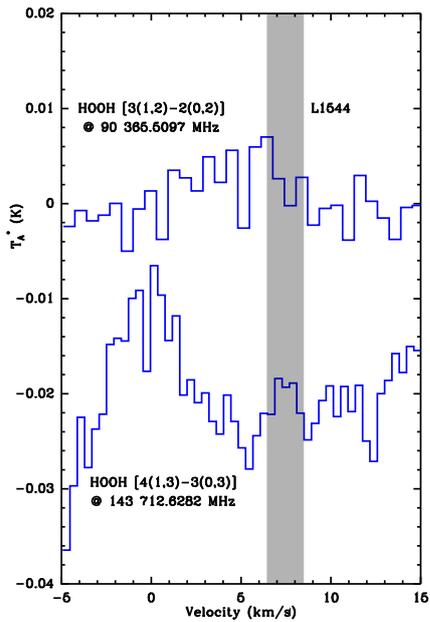
Fig. A.3. Frequency region with HOOH transitions (gray) toward L1544 (frequency-switching mode). Both spectra have the same intensity scale, but the lower spectrum is plotted with an intensity offset.